



Charge-carrier relaxation in sonochemically fabricated dendronized $\text{CaSiO}_3\text{-SiO}_2\text{-Si}$ nanoheterostructures

Rada Savkina¹ · Aleksey Smirnov¹ · Svitlana Kirilova¹ · Volodymyr Shmid² · Artem Podolian² · Andriy Nadtochiy² · Volodymyr Odarych² · Oleg Korotchenkov²

Received: 5 January 2018 / Accepted: 2 April 2018
© Springer-Verlag GmbH Germany, part of Springer Nature 2018

Abstract

We present systematic studies of charge-carrier relaxation processes in sonochemically nanostructured silicon wafers. Impedance spectroscopy and transient photovoltage techniques are employed. It is found that interface potential in Si wafers remarkably increases upon their exposure to sonochemical treatments in Ca-rich environments. In contrast, the density of fast interface electron states remains almost unchanged. It is found that the initial photovoltage decay, taken before ultrasonic treatments, exhibits the involvement of shorter- and longer time recombination and trapping centers. The decay speeds up remarkably due to cavitation treatments, which is accompanied by a substantial quenching of the photovoltage magnitude. It is also found that, before the treatments, the photovoltage magnitude is markedly non-uniform over the wafer surface, implying the existence of distributed sites affecting distribution of photoexcited carriers. The treatments cause an overall broadening of the photovoltage distribution. Furthermore, impedance measurements monitor the progress in surface structuring relevant to several relaxation processes. We believe that sonochemical nanostructuring of silicon wafers with dendronized CaSiO_3 may enable new promising avenue towards low-cost solar energy efficiency multilayered solar cell device structures.

Keywords Cavitation · Silicon · Nanoheterostructure · Surface photovoltaic effect

Introduction

In recent years, calcium silicate (CaSiO_3) has been given an increasing attention for its promising applications based on its good bioactivity, biocompatibility, and biodegradability (Ni et al. 2007; Pan et al. 2016). At high enough pressures, it is believed to have crystallized with a perovskite structure and is, therefore, referred to as Ca–Si–perovskite. At lower pressures, Ca–Si–perovskite is not stable and converts to wollastonite. The tremendous improvements in high-quality film formation techniques and compositional engineering of perovskite materials over the past 5 years have led to rapid improvements in the power conversion efficiency of perovskite solar cells (Yang et al. 2015). Although solar-to-electric conversion efficiencies of up to 18% have been reported for

perovskite solar cells (Jeon et al. 2015), developing technologies further to achieve the efficiencies near theoretical values (> 30%) continues to be an important challenge in making the solar cell industry economically competitive.

The largest light loss mechanism for the perovskite/silicon solar cell is reflection. The majority of this reflection can be attributed to the sets of layer interfaces (Grant et al. 2016), as the large index contrasts between the adjacent layers results in high Fresnel reflection. To increase light absorption within the silicon layer, a scattering surface can be introduced at the inter-layer interface. A number of textured surfaces, such as random pyramids and random spherical caps, can be formed by a number of processes (Baker-Finch et al. 2012). In this approach, the back Si surface is assumed to scatter light, increasing the optical path length of the light within the silicon, as well as allowing for total internal reflection of scattered light from interfaces above the silicon layer. The methodology followed for the light trapping was inspired by Green (2002), where angle-averaged propagation length, front-side reflection, and back-side reflection for the Si layer are calculated numerically.

✉ Rada Savkina
r_savkina@lycos.com; r_savkina@isp.kiev.ua

¹ V. Lashkaryov Institute of Semiconductor Physics, NAS of Ukraine, 41 Nauky av., Kiev 03028, Ukraine

² Taras Shevchenko National University of Kyiv, 64/13, Volodymyrska Street, Kiev 01601, Ukraine

In our previous works (Savkina et al. 2015, 2016), we have shown that the cavitation processing of the silicon samples, providing extremely high impact pressures, has resulted in the essential change of the surface morphology as well as optical and structural properties of silicon surfaces. After $15 \div 30$ min of sonication, inside the structured region, nano- and subnanoscale objects as well as dendrite-like objects were revealed. The investigation of the chemical composition and optical properties of the ultrasonically structured silicon surface has indicated an essential oxidation of the samples after cavitation exposure. In particular, weight percent of the oxygen in the surface of no annealing samples has amounted to 12% (Savkina et al. 2015). Cavitation treatment with post-annealing of Si samples leads to the formation of a complex optical system with transition layers, whose refractive index and extinction coefficient are closed to the optical parameters of SiO_2 and SiN_x compounds (Savkina et al. 2015). A possibility of the fabrication of a composite structure Si/CaSiO_3 , which integrates the nanostructured silicon with calcium silicate, using a simple and low-cost method has also been demonstrated (Savkina et al. 2016).

Moreover, ultrasonically nanostructured regions demonstrate the photoluminescence (PL) response in the range of 500–900 nm. Before annealing, we observed weak PL band in the energy region of 1.7 eV. The sonicated samples after annealing at 980 °C in the atmospheric ambient have demonstrated PL band with an intense peak around 565 nm (2.2 eV) and 750 nm (1.65 eV) (Savkina et al. 2018). Silicon samples, sonicated and annealing at 1100 °C in an inert atmosphere, have demonstrated PL band around 2.2 eV only. Described features could also be related to the radiative processes in silicon oxide. PL bands in the energy range of 2.1–2.3 eV and around 1.7 eV are generally observed in Si-rich SiO_x ($x < 2$) matrixes prepared by various techniques such as PECVD (Kenyon et al. 1996), implantation of silicon into silica (Shimizu-Iwayama et al. 1994) or thermal evaporation of silicon monoxide in vacuum (Nesheva et al. 2002). At that, the properties of the PL bands appear to be very complex and strongly depend on the oxygen content in the SiO_x . The most researchers agree that PL band

at the higher energy (2.1–2.3 eV) is the result of the defect luminescence, possibly from non-bridging oxygen centers or related oxygen vacancies. The lower energy PL band (around 1.7 eV) is associated with radiative recombination of confined excitons.

In this work, we weigh the applicability of dendronized CaSiO_3 -on-silicon interfaces for minimizing light reflection loss at silicon photovoltaic layers. With that in mind, we report the evolution of the surface photovoltage (SPV) magnitude and decay transients over varying sonication conditions of structured silicon surfaces. These surfaces were also monitored using impedance measurements. These studies open new possibilities for improving the quality of multi-layered Si solar cells.

Materials and methods

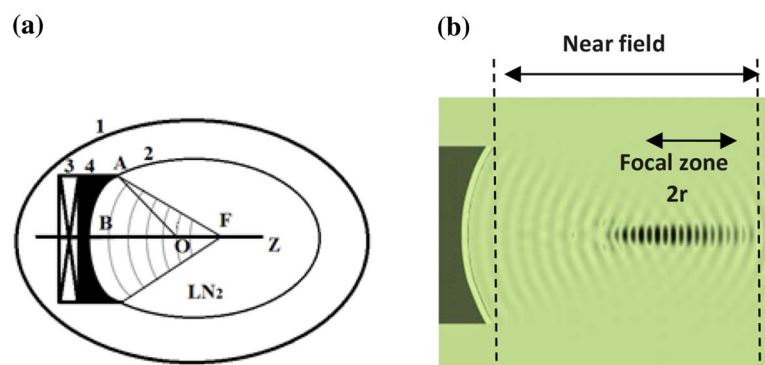
The ultrasonic processing

For cavitation treatments, we used a MHz frequency ultrasound system with focused energy resonator, which was described by Savkina and Smirnov (2010). In our setup, the ultrasonic power was focused onto the sample surface to achieve high operation stability suitable for destructing sample surfaces.

A sketch of our focusing setup is shown in Fig. 1. An oscillating voltage V_{US} applied to a piezoelectric ceramic (PZT-19, 12 mm in diameter, 3 in Fig. 1) causes it to vibrate thus delivering an acoustic power into the liquid nitrogen (LN_2)-filled reactor cavity (Cryo Reactor, 2 in Fig. 1) at an acoustic resonance of 3 and 6 MHz for two different resonators used here. A cylindrical copper lens (4) was used for the acoustic power enhancement.

In our measurements, V_{US} did not exceed 5 V, with a peak value of the acoustic intensity $W_{\text{US}} \approx 1 \text{ W/cm}^2$. Rough estimates in the framework given by Rozenberg (1969) yield the power gain in our acoustic system of about 58. The acoustic matching of the PZT to copper lens satisfied the condition of transparent boundary (transmitting acoustic power

Fig. 1 **a** Schematic image of the Cryo Reactor (top view): stainless steel tank (1) with internal copper cell (2) equipped with an acoustic system—a piezoelectric transducer (3) and copper lens (4); $AO = R_{\text{cu}}$ is a curvature radius, $AF = F$ is a focal distance, $\angle AOB = \beta$, $\angle AFB = \gamma$; **b** image of the calculated acoustic field in the cryogenic liquid



was $\approx 98\%$). The acoustic impedance in liquid nitrogen ($\approx 0.7 \times 10^6 \text{ kg m}^{-2} \text{ s}^{-1}$) is small compared with the impedance of the copper lens ($\approx 3 \times 10^7 \text{ kg m}^{-2} \text{ s}^{-1}$). As a consequence, the ratio of the emitted acoustic power to the dissipated power is about 55%.

We, furthermore, estimated the focal area $2r$ (see Fig. 1b) of our acoustic system as $0.61 \cdot \lambda / \gamma \approx 0.5 \text{ mm}$, where λ is acoustic wavelength and γ is the opening angle of the wave front ($\angle \text{AFB}$ in Fig. 1). Assuming that the transducer pressure is P_0 , the acoustic pressure in the center of the focal zone ($\gamma=0$) can be given as (Rozenberg 1969)

$$P_F = P_0 \sqrt{\frac{4F}{\lambda}} \gamma, \quad (1)$$

where F ($\sim 9 \text{ mm}$) is the focal distance. We estimate $P_F \approx 8 \text{ bar}$. The samples were freely levitating near the focal zone. The effective cavitation nucleation was achieved by elevating the operating temperature in the US reactor to match the boiling point of nitrogen.

Samples

Silicon wafers grown by the liquid-encapsulated Czochralski method were cut into $5 \text{ mm} \times 10 \text{ mm}$ plates from the boron-doped (100)-oriented p-type silicon wafers with the diameter of 76.2 mm . They were cleaned in ethanol for 10 min and then placed in ddH₂O (water for analytical laboratory use, ISO 3696:1987). XRD patterns of the wafer samples denote the existence of a small amount of amorphous phase on the Si surface revealed by a broad bump intensity distribution in the range of $2\theta = 20^\circ\text{--}30^\circ$. We believe that this layer is removed during the sonication, so that the structured region is totally built into the crystalline silicon region.

One cavitation treatment step was typically performed in cryogenic liquid during 30–35 min, yielding a set #1 of samples used here (marked SiN5 and SiN6 in Table 1). Another two sets of samples (2 and 3 in Table 1), which are marked below as Si-26-06 and Si-24-12, were obtained in liquid nitrogen by adding a considerable amount of calcium to the reactor vessel. Here, we present the results obtained with the powder of gluconic acid calcium salt ($\text{C}_{12}\text{H}_{22}\text{CaO}_{14}$) placed into the vessel. Decomposing the salt in the cavitation processing forms calcium oxide (CaO), carbon (C),

carbon dioxide (CO_2), and water (H_2O). After sonication, a part of the set #1 samples was annealed in the atmospheric ambient at 980°C for 1 h (set #2). Another samples were annealed in the nitrogen vapor at 1100°C for 2 h (set #3). After the treatments, samples were cooled down to a room temperature in the furnace.

Equilibrium charge transport

was investigated by the impedance spectroscopy. Impedance characteristics of the samples were studied using the precision impedance meter Z-3000X within the frequency range of 1 Hz to $3 \times 10^6 \text{ Hz}$ with the RF signal amplitude of 120 mV. Using the impedance technique, data equivalent to the real and imaginary parts of complex electrical values were measured as a function of the frequency of the applied electric field. The impedance is

$$Z = \frac{V(t)}{I(t)} = \frac{V_0}{I_0} e^{i\varphi} = |Z|(\cos \varphi + i \sin \varphi) = Z' + iZ'', \quad (2)$$

where $V(t) = V_0 e^{i(\omega t + \varphi_V)}$ and $I(t) = I_0 e^{i(\omega t + \varphi_I)}$ are the time-varying voltage and current, respectively, ω is the frequency, φ_V and φ_I are the voltage and current phase shifts, respectively, and $\varphi = \varphi_V - \varphi_I$. From the number and dimensions of the semicircles observed in the complex plane as $Z' - Z''$ plot, the physical phenomena occurring at the interfaces, such as diffusion and recombination processes, are uncovered here. The impedance measurements were performed in the G-Cp (parallel conductance and capacitance) configuration using Au plates as blocking electrodes.

Nonequilibrium charge transport investigations

SPV transients

SPV transients were measured in the capacitor arrangement using a red light-emitting diode (LED) with a pulsewidth of 100 ns as an excitation source. Details of our setup are given elsewhere (Podolian et al. 2010). A parallel plate capacitance was formed between a metal grid electrode with transparency of about 30% and the structure, separated by a mica insulating foil with a thickness of about $20 \mu\text{m}$. A 1-G Ω load resistor, a high-impedance buffer cascade (input

Table 1 Preparation steps of investigated samples

Sample set number	1		2	3
Sample name	SiN5	SiN6	Si-26-06	Si-24-12
Cavitation treatment in LN ₂	30 min	30 min \times 2	30 min + Ca	30 min + Ca
Post-annealing	—	—	60 min	120 min
Temperature	—	—	980 $^\circ\text{C}$	1100 $^\circ\text{C}$
Ambient	—	—	Air	N ₂ vapor

resistance $10^{13} \Omega$ and output resistance 50Ω) based on a field-effect transistor, and a sampling digital oscilloscope were used in the measurements. The measuring circuit was carefully screened to ensure that the experimental system was not susceptible to electronic pickups or ground loop effects. The scanning SPV apparatus provided surface maps of both the photovoltage magnitude and decay time with a $100\text{-}\mu\text{m}$ spatial resolution, as discussed elsewhere (Nadtochiy et al. 2011).

SPV temperature dependences

The temperature evolution of SPV was also measured in the capacitor arrangement. A measuring capacitor p-Si-mica was assembled, onto a rear side of which a semitransparent conductive layer of the antimony-doped tin oxide $\text{SnO}_2\text{:Sb}$ was deposited. An ohmic contact on ultrasonically structured p-Si was formed by fusing indium. SPV signal was recorded using a storage oscilloscope. The light source was a flash lamp generating a pulse of $10 \mu\text{s}$ in width with an intensity of 10^{21} photons/($\text{cm}^2 \text{ s}$) in the mode of single pulses or their trains with a frequency of 1 Hz. The temperature dependences of SPV were measured as the temperature was lowered from 300 to 100 K when the measuring capacitor was placed into a cryostat maintained under a vacuum of 10^{-3} Pa. The

capacitor temperature was increased using an electric heater installed in the cryostat.

Results and discussion

Surface characterization

The initial surface was found to be essentially flat, having a roughness of less than 1 nm, as measured by atomic force microscopy (AFM, Digital Instruments NanoScope IIIa) over several randomly chosen areas of $40 \times 40 \mu\text{m}^2$. After 10 min treatments, the root-mean-square (RMS) surface roughness and the average height deviation (R_a) are found to be ~ 5 nm and ~ 3.8 nm, respectively. The surface roughness increases up to $\text{RMS} \approx 33$ nm and $R_a \approx 27$ nm after 20 min treatment times, while the values $\text{RMS} \approx 98$ nm and $R_a \approx 79$ nm are obtained with the surfaces treated for 35 min. The analysis of the surface height histograms can separate the several groups of structures with the typical heights ~ 30 nm and ~ 70 nm after 35 min treatment (see AFM images in Fig. 2).

It is necessary to point out that samples sonicated in Cryo Reactor at high enough acoustic powers with an addition of a considerable amount of calcium exhibit dendronized

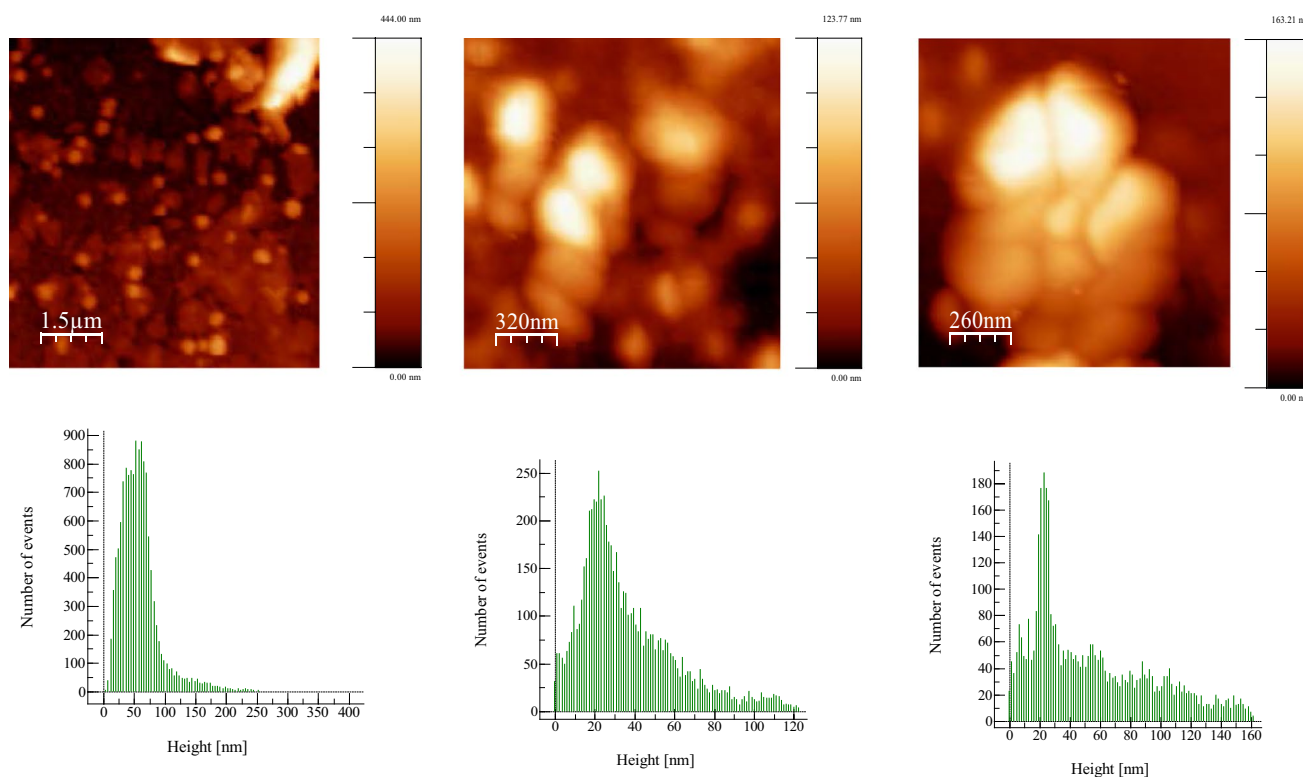


Fig. 2 Typical AFM images of the nanostructured surface after the (1–6) MHz sonication (15 W/cm^2) with corresponding histograms for Si samples. Images were processed with WSxM software (Horcas et al. 2007)

structures (see Fig. 3a). The increase in the processing time results in the appearance of the features with crystal symmetry, as shown in Fig. 3b. Figure 3c illustrates the changes in the silicon surface after post-sonication annealing. It is seen that denser surface roughness features are introduced via the sonication. Similar results have also been reported and interpreted by the fact that the surface of bulk silicon is effectively functionalized and composite structure features, such as CaO-SiO_2 , arise on Si (Savkina et al. 2016, 2018).

Impedance spectroscopy

Figure 4a shows the complex impedance plane plots of our samples. They are semicircle shaped. The arrow shows the direction of the increase in frequency. Symbols are the experimental data and solid lines are the best fit curves to the measured spectra using the modified equivalent circuits of Fig. 4b, c, which are obtained with the EIS spectrum analyzer (<http://www.abc.chemistry.bsu.by/vi/analyser/>). The fitting was performed using the values of the circuit elements, as given in Table 2. The conventional equivalent circuits used for our samples have series resistance R_1 followed by the parallel circuit of CPE_1 , series $R_2\text{--}C_1$, and the parallel circuit $R_3\text{--}C_1$.

The resistance R_1 is usually associated with the contact resistance. However, since in our case $R_1 \gg 1 \Omega$, we believe that R_1 combines both the contact and the bulk material resistance. CPE is the constant phase element with impedance:

$$Z_{\text{CPE}} = \frac{1}{A(i\omega)^n}, \quad (3)$$

which is used to accommodate the nonideal behavior of the capacitance which may have its origin in the presence of more than one relaxation process with similar relaxation times (Bisquert and Fabregat-Santiago 2010). The parameter n estimates the nonideal behavior having a value of zero for pure resistive behavior and is unity for capacitive behavior. In our case, n is somewhat smaller than unity (see Table 2), whereas the series $R_2\text{--}C_1$ and the parallel circuit $R_3\text{--}C_1$

correspond to the charge transport in the space-charge region of the sonochemically structured subsurface layer.

Frequency dependence of the impedance $|Z|$ and phase shift θ in our samples is shown in Fig. 4d, e, respectively. The frequency dispersion is not observed within the range of 10 Hz–10 kHz (see Fig. 4d). The experimental data give a cut-off frequency (the frequency, which characterize a boundary between a passband and a stopband) of about 8.5 kHz in Si-26-06, which corresponds to the time constant of about 0.1 ms. The cut-off frequency of ≈ 18 kHz (with the time constant of $\approx 56 \mu\text{s}$) is obtained in Si-24-12.

Based on the impedance measurements, we thus conclude that the set #2 and #3 samples exhibit a capacitance-type impedance, which can be associated with several charge-carrier relaxation processes. At least two of them can be revealed by the two different cut-off frequencies, as shown in Fig. 4d.

SPV temperature dependences and transients' investigations

It is widely known that the SPV signal formed due to charge separation in the surface space-charge layer of p-Si is negative (Mandelis 2005; Munakata 2007; Angermann 2008), as was the case in our measurements. The temperature dependences of SPV taken in the set #2 and #3 samples are shown in Fig. 5a. The measured SPV magnitude can be directly related to the opposite-in-sign interface $p\text{-Si}$ potential, $\text{SPV} = -\Pi_s$. As evidenced by the data of Fig. 5a, the interface potential increases with decreasing temperature in all samples, which may originate from the charging of fast interface electron states by holes, as the Fermi level in bulk p-Si shifts towards the valence band with decreasing the temperature.

The positive interface potential $-\Pi_s$ means that electrons are accumulated near the surface of the Si wafer, forming the depletion layer in the space-charge region upon sonicating the samples, which in turn bends the near-surface energy bands downwards (inset in Fig. 5a). On the basis of the temperature dependence of the interface potential

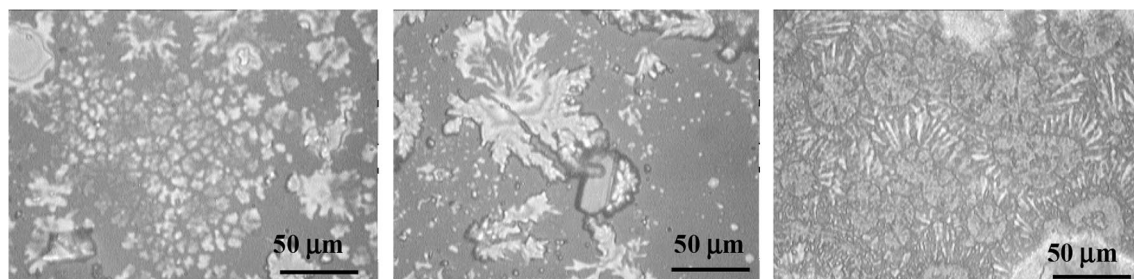


Fig. 3 Optical micrographs of sample surfaces (set #2) exposed to the acoustic cavitation (at 3 MHz) in Cryo Reactor with an addition of Ca during 15 min (a), 30 min (b). Panel c displays the surface in (b) annealed for 1 h at 980 °C (sample Si-26-06)

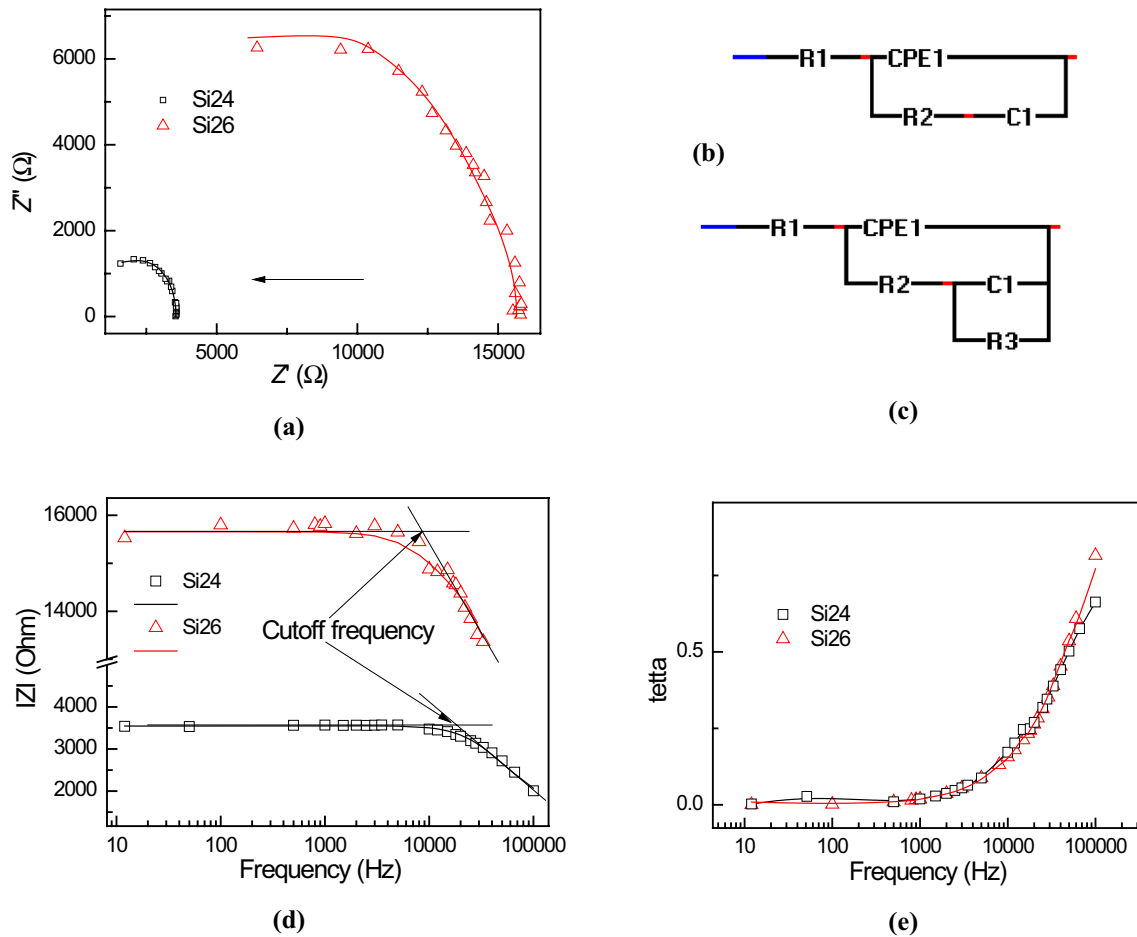


Fig. 4 **a** Nyquist plots showing the complex impedance associated to the sample Si-26-06 (triangles) and Si-24-12 (circles) surfaces; **b** and **c** equivalent electrical circuits representing the interface behavior between the CaO–SiO₂ species and Si wafer for samples Si-24-12 and

Si-26-06, respectively; **d** and **e** changes in the frequency dependent impedance $|Z|$ and the phase shift θ , respectively, in samples Si-24-12 and Si-26-06

Table 2 Values of the equivalent electrical circuit parameters denoted in Fig. 4b, c

Samples	R1 (Ω)	R2 (kΩ)	R3 (kΩ)	C1 (F)	CPE: $Z_{CPE} = A^{-1} (i\omega)^{-n}$		$\tau_1 = R2C1$	$\tau_2 = R3C1$
					A	n		
Si-26-06	200	2.1	1.2	2.4×10^{-9}	5.7×10^{-10}	0.98	$\sim 5 \mu s$	$\sim 3 \mu s$
Si-24-12	1700	14	—	10^{-4}	4×10^{-10}	0.93	$\sim 1.4 s$	—

$-\Pi_s(T)$, we can calculate the temperature dependence of the subsurface charge in space-charge region (Primachenko and Snitko 1988):

$$Q_{sv}(T) = \sqrt{2}qn_iL \left[\frac{n_i}{n} \left(e^{\frac{q\Pi_s(T)}{kT}} - 1 \right) + \frac{n_i}{n} \left(e^{-\frac{q\Pi_s(T)}{kT}} - 1 \right) + \frac{q\Pi_s(T)}{kT} \left(\frac{n_i}{n} - \frac{n}{n_i} \right) \right]^{1/2}, \quad (4)$$

where $L = \sqrt{(\epsilon kT)/q^2 n_i}$, n is a carriers concentration in Si at certain temperature T , which is determined by Hall

measurements; n_i is an intrinsic concentration of the charge carriers; q is the electron charge; k is Boltzmann's constant; and ϵ is the dielectric constant of Si. The character of the temperature dependence of the subsurface charge in space-charge region is the same as the temperature dependence of the interface potential $-\Pi_s(T)$, i.e., the charge in space-charge region rises with decreasing temperature in all samples.

Having constructed the dependence $Q_{sv}(\psi_s)$, where $\psi_s = \Pi_s + \Pi_b$, we can determine the density of fast interface electron states near interface N_s in the regions of growth

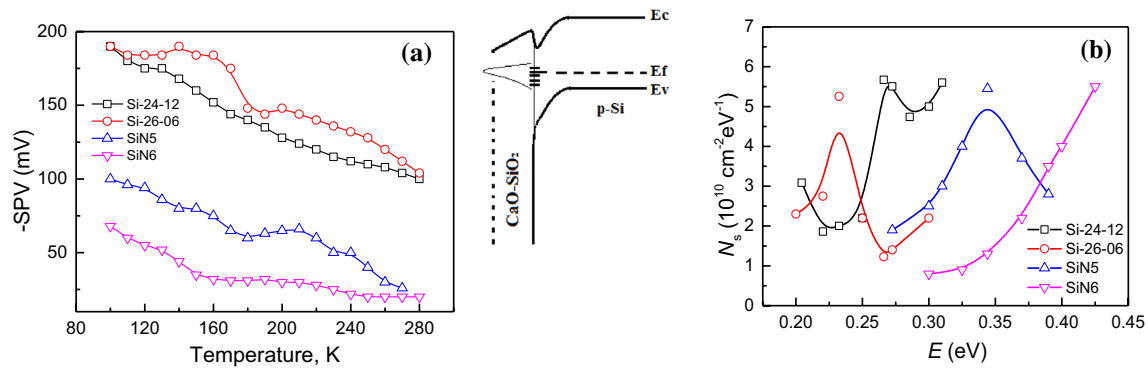


Fig. 5 **a** Temperature dependences of the SPV magnitude in our samples; **b** density distribution of fast interface electron states over energy below the mid-gap. Inset shows schematic diagram of the surface band bending at the CaSiO_3 - SiO_2 -Si interface

of the negative charge as $N_s = |\Delta Q_s| / \Delta(q\psi_s)$. Here, $q\pi_b$ and $q\psi_s$ are a distance between a silicon mid-gap E_g and Fermi level E_F in the bulk and at the surface correspondingly. Our calculation results are shown in Fig. 5b, elucidating nearly identical peak values of N_s in all the samples, which are in the range from 5.6 to $6.3 \times 10^{10} \text{ cm}^{-2} \text{ eV}^{-1}$.

We thus conclude that the interface potential is much greater in the sonochemically structured Si samples treated in Ca-rich environments. Moreover, the peak densities of fast interface electron states in the Ca-rich treated Si shift towards the mid-gap energy in comparison with that reproduced in the samples sonochemically structured without

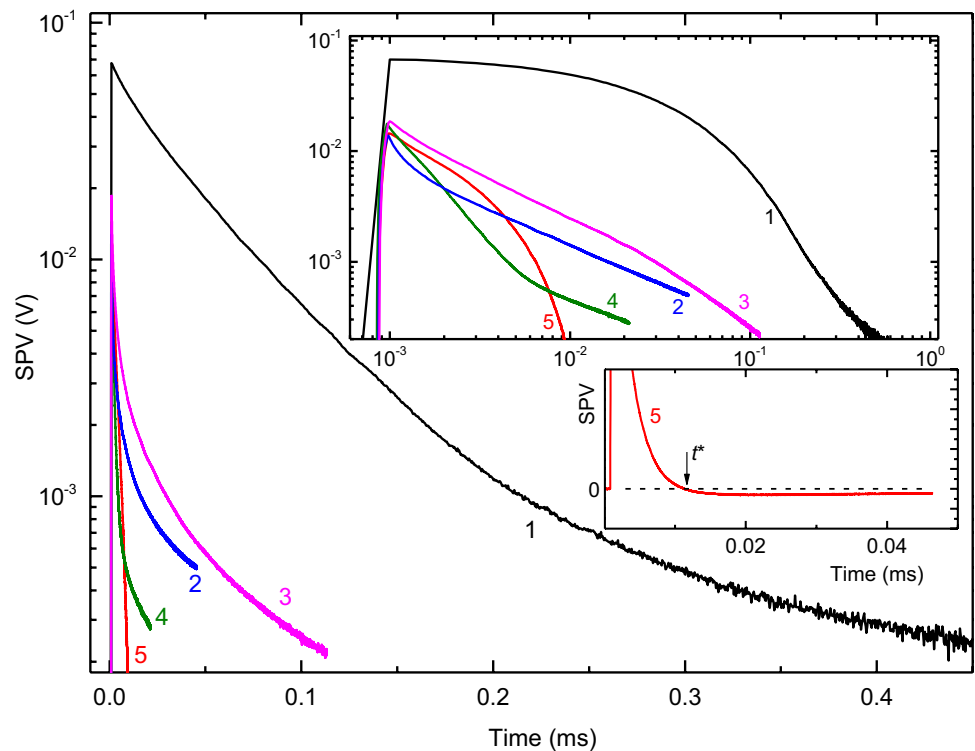
deliberately added Ca. This in turn leads to an increasing recombination rate at fast interface electron states.

Typical SPV transients, which are shown reversed in sign in Fig. 6, exhibit direct evidence for the involvement of traps and recombination centers. We found that the decay curves can be well fitted to a triple-exponent form:

$$U = U_1 e^{-t/\tau_1} + U_2 e^{-t/\tau_2} + U_3 e^{-t/\tau_3}, \quad (5)$$

indicating the involvement of several mechanism of recombination and trapping centers resulting in effective lifetimes given by τ_1 , τ_2 and τ_3 . These lifetimes are collected in Table 3.

Fig. 6 Time-dependent SPV of Si wafer (1), samples SiN5 (2), SiN6 (3), Si-26-06 (4) and Si-24-12 (5) in the log-linear representation. Upper inset shows the same decay curves replotted on a log-log scale, lower inset enlarges curve 5 in a linear scale. The decays are taken with unfocused 640-nm LED light striking the sample surface, about 5 mm in diameter



The transients can be given a clear physical interpretation, which is as follows. The initial decay in Si wafer, when the injected carrier concentrations are large compared with the density of the trapping centers N_t , is nearly simple exponentials with the dominating time constant τ_1 in Table 2. The final decay at times greater than ≈ 0.2 ms (curve 1 in Fig. 6), when the injected concentration is small compared with N_t , is also simple exponentials of greater time constant τ_2 determined by N_t (Baicker 1963).

The consequent cavitation treatments used here lead to significant shortening of the SPV decay (curves 2–5 in Fig. 6). Obviously, the decay speeds up in curves 2 and 3 taken from the surfaces sonicated for 30 (curve 2) and 60 (curve 3) min. This behavior can be attributed to activation of the wafer surface dangling bonds, as the cavitating bubbles are capable of locally removing the surface oxide layer developing the dangling bonds on the bare Si surface. This increases the number of fast recombination centers, thus accelerating the SPV decays.

Treating in the $C_{12}H_{22}CaO_{14}$ environment further accelerates the decays, as seen in curves 4 and 5 in Fig. 6. It is also obvious that the SPV signal taken in sample Si-24-12, which is annealed at elevated temperatures (1100 °C) in the nitrogen ambient, gets smaller in magnitude and initially decays slower (curve 5 compared with curve 4 in upper inset of Fig. 6). Furthermore, at time instants greater than $t^* \approx 0.01$ ms, the SPV sign changes to positive in sample Si-24-12 (lower inset of Fig. 6). Therefore, the SPV decay reproduced in this sample can be decomposed into three transients with positive and negative values of the partial amplitude factors U_1 , U_2 , and U_3 in Eq. (5). This suggests that, in the sample annealed at elevated temperatures in the nitrogen ambient, there is a competitive path of separating photoexcited electrons and holes, which indicates the need for further study and will not be discussed here anymore. The decay acceleration after treating in the $C_{12}H_{22}CaO_{14}$ environment can be related to the above mid-gap shift of the peak densities of fast interface electron states. In accord, treating in the $C_{12}H_{22}CaO_{14}$ environment and annealing at elevated temperatures (1100 °C) in the nitrogen ambient lead to somewhat smaller shift values for the peak density

given in the inset of Fig. 5. The recombination rate at fast interface electron states concomitantly decreases, which is manifested by slower decays in sample Si-24-12 (see Table 3).

Surface mapping of the SPV signal indicates that, both before and after the cavitation treatments, the photovoltage magnitude is markedly non-uniform over the wafer surface; see Fig. 7. Comparing panels (b) to (d) with panel (a) shows that the cavitation treatment causes an overall quenching of the SPV signal. Structuring wafer surface decreases the SPV magnitude from about 1–10 mV in panel (a) to about 0.1–1 mV in panel (b), which can be thought of as arising from the increased number of fast recombination centers suggested above. The cavitation treatment in the Ca-rich environment does not appear to quench the overall SPV magnitude, rather broadening the probability distribution to smaller magnitudes, as evidenced by narrow spikes in the distribution functions seen in panels (c) and (d) in Fig. 7. This result implies the occurrence of distributed surface sites due to formation of dendronized $CaSiO_3$ species, which affect the distribution of photoexcited charge carriers.

Conclusions

Systematic study of charge-carrier relaxation processes in sonochemically nanostructured silicon wafers was carried out. Impedance spectroscopy and surface photovoltage techniques were applied. It was found that sonochemically structured silicon samples are characterized by capacity-type impedance and demonstrate more than one charge-carrier relaxation process after treatment in Cryo Reactor and post-sonication annealing. A cut-off frequency characterizing the response of the obtained composite structure is in the range of tens kHz and is depended from the annealing conditions. The electronic properties of layer–substrate interface in the Si-based composite structure were studied and the density of states trapping majority carriers at the layer–substrate interface was estimated. It was found that interface potential for Si samples sonicated with following annealing is appreciably higher than that for Si samples sonicated without annealing, while the densities of fast interface electron states in them are almost identical. The peak densities of fast interface electron states in the Ca-rich treated samples shift towards the mid-gap energy with denser surface roughness features introduced on their surface.

It is found that the initial photovoltage decay, taken before ultrasonic treatments, exhibits the involvement of shorter- and longer time recombination and trapping centers. The decay speeds up remarkably due to cavitation treatments, which is accompanied by a substantial quenching of the photovoltage magnitude. The acceleration of

Table 3 Values of τ_1 , τ_2 and τ_3 obtained by fitting curves 1–5 in Fig. 6 to Eq. 4

Samples	τ_1 (ms)	τ_2 (ms)	τ_3 (ms)
Si wafer (curve 1 in Fig. 4)	11.10 ± 0.04	45.45 ± 0.04	300 ± 3
SiN5 (curve 2)	0.210 ± 0.001	1.520 ± 0.009	10.66 ± 0.05
SiN6 (curve 3)	0.500 ± 0.002	2.85 ± 0.01	22.55 ± 0.06
Si-26-06 (curve 4)	0.180 ± 0.001	0.810 ± 0.002	4.23 ± 0.03
Si-24-12 (curve 5)	0.350 ± 0.001	2.420 ± 0.001	133 ± 3

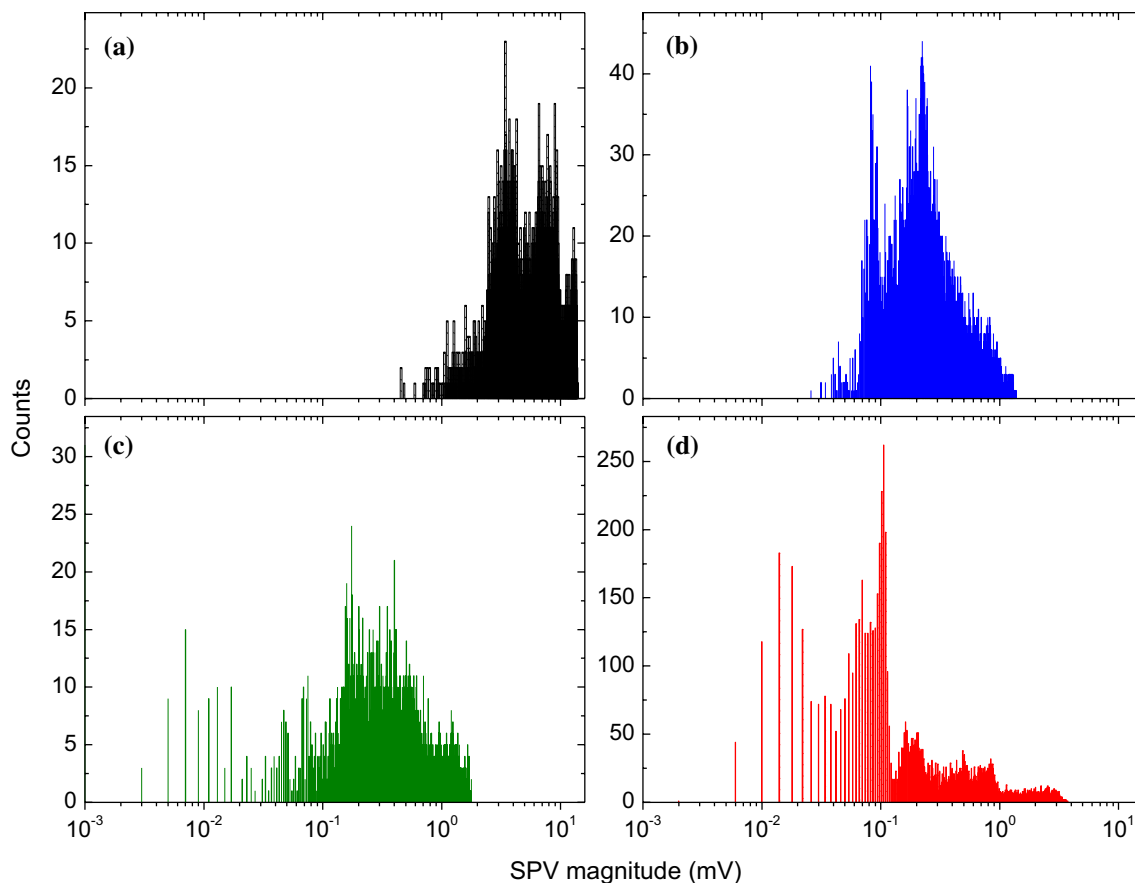


Fig. 7 Probability of occurrences of a particular value of the SPV magnitude in Si wafer **(a)**, samples SiN5 **(b)**, Si-26-06 **(c)** and Si-24-12 **(d)**, which are measured by surface mappings of the SPV decays. The decays are taken with a LED light focused to a spot of 100 μm in diameter

the decays after cavitation treatments in the $\text{C}_{12}\text{H}_{22}\text{CaO}_{14}$ environment and subsequent annealing can be explained by increased recombination rate at fast interface electron states due to the mid-gap-energy shifted peak densities. Importantly, annealing in N_2 vapor environments leads to smaller shift values for the peak density, which results in smaller carrier recombination rates at fast interface electron states. It is also found that, before the treatments, the photovoltage magnitude is markedly non-uniform over the wafer surface, implying the existence of distributed sites affecting distribution of photoexcited carriers. The treatments cause an overall broadening of the photovoltage distribution.

We believe that denser surface roughness features produced by the sonication in $\text{C}_{12}\text{H}_{22}\text{CaO}_{14}$ environments together with increased interface potential can be considered as an important advantage of this technique for producing effective solar cells. Quenching of the recombination rate at fast interface electron states takes on special significance for the solar cell performance.

References

- Angermann H (2008) Passivation of structured p-type silicon interfaces: effect of surface morphology and wet-chemical pre-treatment. *Appl Surf Sci* 254:8067
- Baicker JA (1963) Recombination and trapping in normal and electron-irradiated silicon. *Phys Rev* 129:1174–1180
- Baker-Finch SC, McIntosh KR, Terry ML (2012) Isotextured silicon solar cell analysis and modeling 1: optics. *IEEE J Photovolt* 2:457–464. <https://doi.org/10.1109/JPHOTOV.2012.2206569>
- Bisquert J, Fabregat-Santiago F (2010) Impedance spectroscopy: a general introduction and application to dye-sensitized solar cells. CRC Press, Boca Raton
- Grant DT, Catchpole KR, Weber KJ, White TP (2016) Design guidelines for perovskite/silicon 2-terminal tandem solar cells: an optical study. *Opt Express* 24:1454–1470
- Green MA (2002) Lambertian light trapping in textured solar cells and light-emitting diodes: analytical solutions. *Prog Photovolt Res Appl* 10:235–241. <https://doi.org/10.1002/ppp.404>
- Horcas I et al (2007) WSxM: a software for scanning probe microscopy and a tool for nanotechnology. *Rev Sci Instrum* 78:013705–013705-8
- Jeon NJ, Noh JH, Yang WS, Kim YC, Ryu S, Seo J, Seok SI (2015) Compositional engineering of perovskite materials for high-performance solar cells. *Nature* 517:476–480

- Kenyon AJ et al (1996) The origin of photoluminescence from thin films of silicon-rich silica. *J Appl Phys* 79:9291–9300
- Mandelis A (2005) Theory of space-charge layer dynamics at oxide-semiconductor interfaces under optical modulation and detection by laser photocarrier radiometry. *J Appl Phys* 97:083508
- Munakata C (2007) Decay times of impulse surface photovoltages in p-type silicon wafers. *Jpn J Appl Phys* 46:6592
- Nadtochiy A, Podolian A, Korotchenkov O, Schmid J, Kancsar E, Schlosser V (2011) Water-based sonochemical cleaning in the manufacturing of high-efficiency photovoltaic silicon wafers. *Phys Stat Sol C* 8:2927–2930
- Nesheva D et al (2002) Raman scattering and photoluminescence from Si nanoparticles in annealed SiO_x thin films. *J Appl Phys* 92:4678–4683
- Ni SY, Chang J, Chou L, Zhai WY (2007) Comparison of osteoblast-like cell responses to calcium silicate and tricalcium phosphate ceramics in vitro. *J Biomed Mater Res B* 80:174–183
- Pan Y, Zuo K, Yao D, Yin J, Xin Y, Xia Y, Liang H, Zeng Y (2016) The improved mechanical properties of β -CaSiO₃ bioceramics with Si₃N₄ addition. *J Mech Behav Biomed Mater* 55:120–126
- Podolian A, Kozachenko V, Nadtochiy A, Borovoy N, Korotchenkov O (2010) Photovoltage transients at fullerene-metal interfaces. *J Appl Phys* 107:093706
- Primachenko V, Snitko O (1988) Physics of the metal doped semiconductor surface. Kyiv, Naukova dumka, p 232
- Rozenberg LD (1969) Sources of high-intensity ultrasound (ultrasonic technology), vol 1. Springer, Berlin, pp 223–315
- Savkina RK, Smirnov AB (2010) Nitrogen incorporation into GaAs lattice as a result of the surface cavitation effect. *J Phys D Appl Phys* 43(42):425301–425307
- Savkina RK, Smirnov AB, Kryshchuk T, Kryvko A (2015) Sonosynthesis of microstructures array for semiconductor photovoltaics. *Mater Sci Semicond Process* 37:179–184
- Savkina RK, Gudymenko AI, Kladko VP, Korchovy AA, Nikolenko AS, Smirnov AB, Stara TR, Strelchuk VV (2016) Silicon substrate strained and structured via cavitation effect for photovoltaic and biomedical application. *Nanoscale Res Lett* 11:183
- Savkina RK, Smirnov AB, Gudymenko AI, Morozhenko VA, Nikolenko AS, Smoliy MI, Kryshchuk TG (2018) Silicon surface functionalization based on cavitation processing. *Surf Coat Technol* 343:17–23
- Shimizu-Iwayama T, Nakao S, Saitoh K, Fujita T, Itoh N (1994) Visible photoluminescence in Si⁺-implanted silica glass. *J Appl Phys* 75:7779–7783
- Yang WS, Noh JH, Jeon NJ, Kim YC, Ryu S, Seo J, Seok SI (2015) High-performance photovoltaic perovskite layers fabricated through intramolecular exchange. *Science* 348:1234–1237

Publisher's Note Springer Nature remains neutral with regard to jurisdictional claims in published maps and institutional affiliations.